NanoImpact 42 (2026) 100624

Contents lists available at ScienceDirect

NanoImpact

journal homepage: www.elsevier.com/locate/nanoimpact

Research Paper

Multi-scale in-silico toxicological assessment of Ti_3C_2 and Cr_2C MXene nanoparticles at human biological interfaces

Sergio de-la-Huerta-Sainz [a], Valentín Díez-Cabanes [a,b], Pedro A. Marcos Villa [c], Alfredo Bol [b,c], Laura Gómez-Cuadrado [b], Dalia de la Fuente-Vivas [b], Javier Alcodori Ramos [d], Carla F. Martins [e], Inês T. Meireles [e], Ana Rita Alberto [e,f], Santiago Aparicio [a,b,*]

[a] Department of Chemistry, University of Burgos, 09001 Burgos, Spain
[b] International Research Center in Critical Raw Materials for Advanced Industrial Technologies (ICCRAM), University of Burgos, 09001 Burgos, Spain
[c] Department of Physics, University of Burgos, 09001 Burgos, Spain
[d] Processes and Products Safety Unit, Packaging, Transport and Logistics Research Institute (ITENE), 46980, Paterna, Spain
[e] Low Carbon & Resource Efficiency, R&Di Department, ISQ - Instituto de Soldadura e Qualidade, Av. Prof. Cavaco Silva 33, 2740-120 Oeiras, Portugal
[f] NOVA National School of Public Health, Public Health Research Centre, Comprehensive Health Research Centre, CHRC, REAL, CCAL, NOVA University Lisbon, Lisbon, Portugal

ARTICLE INFO

Keywords:
MXenes
Human toxicity
Density functional theory
Molecular docking
Membrane permeability

ABSTRACT

Despite their huge technological interest, practical application of MXene nanomaterials is somehow hampered by their potential toxicity. In this regard, the present work showcases the design and implementation of a full *in-silico* methodology for the toxicological analysis of nanoparticles (NPs) of two MXenes within a human cell environment, employing cost-effective computational approaches to achieve a preliminary hazard estimation in the absence of experimental data. This study combines computational methodologies of very different nature, from Density Functional Theory (DFT) calculations for a full quantum mechanics optimization of the system of interest and thermodynamical approximations like the COSMO-RS methodology for the analysis of the behaviour in membranes, to other, simpler methods like classic electrostatic Monte-Carlo calculations for the interaction with proteins, and machine-learning based methods for the development of simpler yet accurate predictive tools for a broader use. This multi-scale workflow was applied to a compendium of NPs derived from two MXenes of interest, Ti_3C_2 and Cr_2C, to understand the possible harm such materials could cause in the human body. As a result, an extremely low permeability and membrane-crossing potential was observed for the Ti_3C_2 NPs, and very weak and superficial interaction was observed for both MXenes with a library of critical human proteins. Two predictive docking energies models with R^2 of 0.85 were developed, and a low toxicological potential via the considered mechanisms was concluded as a result, thus paving the way of reaching accurate toxicological predictions for a wide range of MXene nanomaterials.

1. Introduction

MXenes are a group of 2D transition metal carbides, nitrides, and carbonitrides (Shao et al., 2020) whose name derive from their general formula $M_{n+1}X_n$, where M references a metallic element, X an element of groups 14 and 15, and *n* an integer number, with n + 1 layers of M atoms are intercalated with n layers of X atoms; some of the typical species are Ti_3C_2, Cr_2C or even mixed metal species like Mo_2TiC_2, to cite a few. These materials have made their debut in the last decade as an alternative to similar systems such as graphene, offering high potential for surface functionalization via the inclusion of functional groups and anchorage of various decorations to fine-tune their properties for each purpose (Anasori and Gogotsi, 2023; Kamysbayev et al., 2020; Thakur and Anasori, 2024; Wang et al., 2016). Ti_3C_2 represents the prototype material since is the most studied and technologically mature MXene, due to a unique combination of stability, conductivity, and surface chemistry. (Naguib et al., 2014) During the last years, the attention Cr_2C MXenes has recently increased due to its magnetic ordering (ferromagnetic or antiferromagnetic depending on terminations), electronic properties (strongly correlated electrons) and enhanced chemical

* Corresponding author at: Department of Chemistry, University of Burgos, 09001 Burgos, Spain.
E-mail address: sapar@ubu.es (S. Aparicio).

https://doi.org/10.1016/j.impact.2026.100624
Received 9 January 2026; Received in revised form 13 March 2026; Accepted 7 April 2026
Available online 14 April 2026

reactivity. (Khazaei et al., 2017).

The abundant transition metals on their composition guarantees a high density of electronic states at the fermi level -the hypothetical energy level that would have a 50% probability of being occupied should the material be in thermodynamical equilibrium (Britannica Editors, 2006). As a result, these materials are inherently metallic, with an excellent electrical conductivity and high potential for energy storage (Pang et al., 2019) in various lithium and sodium-based batteries, which can be improved with functionalization or hybridized with other nanomaterials such as graphene or polymers like PVA, PPy or PANI (Boota et al., 2016; VahidMohammadi et al., 2018). Hybridization of MXenes with other materials also allows them to showcase remarkable mechanical properties close to those observed in graphene and carbon nanotubes, and making them viable for the construction of flexible electrodes capable of withstanding large tensile forces. Some of their most promising applications include supercapacitors (Ghidiu et al., 2014; Lukatskaya et al., 2017; Sun et al., 2014), chemical sensors (Krishnamoorthy et al., 2022; Le et al., 2022; Lemena et al., 2025; Li et al., 2020; Yao et al., 2025), optoelectronic devices (Aleithan and Ahmad, 2025; Liu and Alshareef, 2021; "MXene Nanosheets For Future Optoelectronic Devices,", 2020) and even as electrodes for water purification (Mansoor et al., 2022; Ren et al., 2015).

Taking all these potential applications into account, the synthesis of these materials is scaling up, but so it does the potential hazards on both its production and use. Due to that, a proper toxicological assessment is needed to ensure the safety of both workers and end users. It is known that these materials can induce cellular responses such as oxidative stress, inflammation, and genotoxicity (Lin et al., 2024), but the material availability and the various toxicity mechanisms and factors at play lead to fragmented nanosafety data that are often challenging to compare (Lim et al., 2021). For example, reports on Ti_3C_2 ~~flakes~~ nanoparticles and astrocytes (Boufidis et al., 2025) show ~~that there are~~ no remarkable changes in cell viability, with a mere membrane aggregation but not disruption of any activity. On other cases, the sharp MXene edges are known to cleave bacteria and generate the formation of Reactive Oxygen Species (ROS) from light (Purbayanto et al., 2022), and on vegetal cells it has been observed their disruption to nutrient and light access via surface coating (Nawaz et al., 2025). Lastly, MXenes have been shown to induce cytotoxicity preferentially in cancer cell models (A375 and MCF-7), sparing normal cell lines such as HaCaT and MCF-10 (Vasyukova et al., 2022) and underscoring the potential of these materials for broad-ranging applications, particularly in targeted drug delivery. Overall, while normally appearing as biocompatible, there are certain unconventional toxicological mechanisms that end up making MXenes a potential threat and must be addressed.

To help closing this knowledge gap and bypass the material availability limitations, this work proposes a full in-silico methodology based on structural data and various computational methods to study several biological interaction pathways. The complexity of the chemical environments within a living organism makes a perfect in-silico replica impossible, so simplified, isolated models will be used instead. To contextualize these models within realistic scenarios, it will be considered even though the synthesis yields polydisperse multilayer systems on the microscale, small nanoparticles can be unintentionally generated during the various production stages and released into the air. Due to this small size, they have the highest potential for biological interaction, and thus being a fitting target for this toxicological in-silico study. As a matter of fact, the reactivity and potential toxicity of such nanostructures can be fine-tuned through their size and exposed terminations (Diez-Cabanes and Pastore, 2021).

Likewise, although real MXenes often exhibit surface terminations (–OH, —O, —F) arising from etching and aqueous processing, the present work considers pristine carbides as a controlled baseline to isolate the contribution of the core MXene chemistry. The phenomena responsible for these surface coverings depend highly on the surrounding medium and often take place on longer timescales, and may be explored in follow-up studies with more focus on the solvent effects and reactivity. Instead, the current framework serves to define a clean reference state upon which more complex and experimentally representative MXene systems can be incorporated in future work.

Of all the various species of MXenes known, this work was centred around two common ones that act as representatives: Ti_3C_2 and Cr_2C. The effect of the metal is probably the most relevant, as titanium-based MXenes are presented as biocompatible, while chromium-based ones show more toxicological concern. However, the cost of simulating the bulk materials themselves would be unaffordable, and a sizeable collection of NPs, cut from the crystalline materials in various shapes and sizes, will be used instead. To achieve this, the Density Functional Theory (DFT) will be the main calculation method, as it offers a good balance between cost, speed and accuracy, and makes the calculations of hundreds of atoms a rather quick achievement. Through this, the NPs will be relaxed into a more stable geometry rather than the rigid and perfect layered structure of the bulk MXene.

Two different interaction mechanisms will be considered in this work: first, the interaction with cell membranes, as the formation of aggregation layers on the cell surface is a well-established toxicological phenomenon; second, the interaction with proteins to check their viability as enzymatic poisons and disruptors of various metabolic pathways, each mechanism with a different workflow. Lastly, the obtained results from both pathways will be used as training data for the development of Machine Learning (ML) based predictive models, to condense this computational workflow into a user-friendly simpler tool.

It is worth mentioning that this study relies solely in computational data, without any in vivo nor in vitro measurements. While experimental validation is a crucial component in nanotoxicology, the novelty of these metals, their limited availability and the lack of standardized biological assays makes an experimental-computational study very challenging as of today. Therefore, this study instead aims to be more of a predictive framework to generate hypothesis, prioritizing NP geometries and guiding future experimental measurements, always keeping in mind the already existing experimental observations when it comes to Ti-based MXenes low cytotoxicity and higher Cr-based MXenes reactivity (Boufidis et al., 2025; Wu et al., 2020). As such, the outputs of this paper should be regarded as a robust and mechanistically grounded baseline for designing targeted toxicity assays and prioritizing risk-assessment studies.

2. Materials and methods

The present work integrates, at a high level, multiple computational techniques into an unified multi-scale workflow designed to characterise MXene NPs from first principles up to biological interaction. The methodology includes quantum-chemical modelling, membrane and protein interaction simulations, and machine-learning analysis into a multi-scale workflow, described in detail in the following sections.

2.1. MXene nanoparticle optimization

2.1.1. Bulk relaxation

The starting point of this work was the structural analysis of the bulk structures, i.e., the crystalline configurations of the MXenes selected, Ti_3C_2 and Cr_2C in this study. An infinite monolayer of both materials was constructed from the crystallographic data provided by the Materials Project database (Jain et al., 2013), both with a similar hexagonal lattice, and using the original lattice *a* and *b* parameters of 3.07 Å for Ti_3C_2 (entry mp-1,094,034) and 2.82 Å for Cr_2C (entry mp-1,226,378) as starting point for further relaxation, with a value for *c* of 20 Å to avoid interlayer interactions and obtain a proper isolated 2D system. These initial structures were optimized via DFT methods, more precisely by means of the planar waves strategy using the GPAW software package on its version 25 (Hjorth Larsen et al., 2017; Mortensen et al., 2024), as it is designed precisely for periodic materials and gives net parameters and

binding energies matching the experimental results (Jain et al., 2013). Both materials were optimized considering exchange-correlation interactions via generalized gradient approximation (GGA) in the Perdew-Burke-Ernzerhof (PBE) functional. (Perdew et al., 1996) The electron wave function was then calculated using an expansion in plane-waves with a cutoff energy of 800 eV. It is worth mentioning that this optimization of the bulk materials was conceived as an initial pre-optimization in order to reduce the computational load on further calculations, and not as study system themselves.

2.1.2. Nanoparticle models

Since the bulk material was not a suitable candidate for mimicking the interaction with large finite molecules such as proteins, or other extensive systems like membranes, the crystalline structure of MXenes served as the basis of constructing a wide library of NPs, varying in shape and size. Three different shapes were considered: triangular (T), rhombic (R) and hexagonal (H), constructed via the repetition of the corresponding unit cells in the appropriate fashion; these particularly shapes are representative of the most common cases in which the material hexagonal lattice can cleave and fragment. A total of ten sizes were considered for each shape, using them as the code for the labelling of each NP. For example, the R5 NP would have a rhombic shape, and a total of 6 (5 + 1) unit cells per edge, or 5 if the corners are assigned to only one. Combining the two types of MXenes, the three shapes and the ten sizes, a total of $2 \times 3 \times 10 = 60$ NPs were considered. The number of atoms of the larger ones, which can easily exceed the thousand, anticipated that not all of them would be viable for the proposed computational approaches. For simplicity, all nanoparticles were considered and treated as neutral for a better representation of the starting materials.

The NPs obtained from the relaxed infinite MXene were further optimized with DFT to account for the higher freedom of movement of the atoms at edges and corners. These relaxations were carried out by following a previously established method to get realistic NP structures (Diez-Cabanes et al., 2021). Within this approach geometry optimizations were performed within the DFT framework by using PBE exchange–correlation functional and Grimme's D3 correction to treat the empirical dispersion (Grimme et al., 2010). Periodic boundary conditions were applied, and a mixed Gaussian and plane-wave basis set approach, as implemented in the CP2K package, was employed (Hutter et al., 2014). To prevent spurious interactions between periodically replicated NPs, the simulation cell was constructed to ensure a minimum vacuum separation of 15 Å between neighbouring images. The electronic structure was described using a double-ζ valence plus polarization (DZVP) basis set, with an auxiliary plane-wave energy cutoff of 500 Ry, while core electrons were treated using Goedecker–Teter–Hutter (GTH) pseudopotentials (Goedecker et al., 1996).

Note that the use of such basis set (DZVP) represents the best compromise between accuracy and the computational cots derived from estimating the electronic structure of such large systems (more than 1300 atoms). On the top of that, the computed atomic charges (which are indeed required for the docking simulations) with DZVP basis were identical to those calculated with more accurate basis sets such as TZVP, as it has been demonstrated by computing the root-mean-square-difference (RMSD) between the charges calculated with both DZVP and TZVP basis sets. The RMSD values for the smallest NPs of each morphology for both Ti_3C_2 and Cr_2C nanomaterials are collected in Table S1. As a matter of fact, the almost negligible RMSD values (in the order of few 10^{-3} e^-) corroborated the suitability of our methodology to compute accurate atomic charges.

Lastly, in order to obtain the *.cosmo* files required by the COSMO-RS (Eckert and Klamt, 2002; Klamt, 1995; Klamt et al., 1998; Schwö et al., 2020) methodology, a single point calculation was performed employing Gaussian 16 (Frisch et al., 2016), software which includes this feature, in contrast to CP2K. The calculations were executed using a BP86 functional and a Triple Zeta Valence Polarized (TZVP) basis set. The main strategy behind the COSMO-RS model is the computation of a surface screening charge around the molecule, called the σ-surface, considering the system is within an infinite conductive continuum medium, which by default and in this work in particular, is water. This surface charge represents the spatial interaction between the solute and the solvent, yielding as a result a charge distribution, called the σ-profile, that acts as a starting point to calculate the chemical potential, and from that, many other thermodynamical properties.

2.2. Membrane interaction

The membrane interaction studies were carried out employing COSMOTherm, 2024 (BIOVIA COSMOtherm, 2026), using the available Ti_3C_2 and Cr_2C *cosmo* files as solute components. For the membrane models, a total of four pure lipidic bilayers were employed, all constructed from common membrane phospholipids (DMPC: dimyristoylphosphatidylcholine, DOPC: dioleoylphosphatidylcholine, POPC: palmitoyloleoylphosphatidilcholine, and SOPC: stearyloleoylphosphatidilcholine, whose relaxed structures can be seen in Fig. 1), optimized using the Turbomole software (Balasubramani et al., 2020; TURBOMOLE V7.8 2023, 2026) considering a water/lipid ratio of ~~31~~ 30 on both sides of the membrane. These membranes were built with a basic MD simulation of 30 ns at 303 K using the Charmm36 potential to allow the molecules to relax into a more stable spatial arrangement (Jakobtorweihen et al., 2013).

The permeability studies were performed considering a set of temperatures ranging from 0 °C to 50 °C for all available NPs and membrane combinations. On each calculation, the Ti_3C_2 and Cr_2C NPs, acting as the solute, will be inserted within the membrane at various depths, assigning the 0 value to the bilayer centre, and extracting the stability of each case via the Gibbs free energy, considering the interactions between the σ-surfaces of both NP and phospholipid. The solute distribution -the likelihood for the solute to be at a given depth-, partition coefficient and diffusion coefficient were the main outputs used to understand the NPs behaviour, which determines the solute's potential for crossing the membranes.

2.3. Protein interaction

The protein interaction studies were carried out using the Autodock 4.2.6 docking software (Morris et al., 2009; Santos-Martins et al., 2014), along with the MGLtools 1.5.7 package (MGLTools, 2011) on a supporting role for the generation of the necessary molecular files and commands. Although Autodock normally does not provide the parametrization for transition metal atoms such as Ti or Cr by default,parameters from non-standard atoms can be easily implemented in Autodock parameter files, typically fetched from large compendiums (Draško Tomić, 2024; Tomić et al., 2024) or derived from high-accuracy calculations (Li et al., 2013; Li and Merz, 2016; Li and Merz, 2014).

MGLtools, with the GUI version of Autodock, was used to convert the molecular files to the required PDBQT format. In the case of the NPs, the Hirshfeld charges obtained from the CP2K output were included. The protein configuration files, on the other hand, were available from previous works (Aguilar et al., 2025; Navarro-Cuñado et al., 2025), developing a protein library containing 97 human proteins that represent common families and participate in key metabolic processes. These proteins are often targets of molecular initiating events (MIE) within the adverse outcome pathway (AOP) framework (Aguilar et al., 2025; Lizano-Fallas et al., 2023). The library also includes a mutant of Bovine Pancreatic Phospholipase due to its relevance in protein structure resolution and enzymatic mechanism determination (Dijkstra et al., 1978; Scott et al., 1990). The full list of proteins and their names can be found in the *Protein library.docx* file at the Supporting Information.

To simulate the docking process was necessary the use of a simulation box of 100 Å surrounding all proteins, in some cases even larger to accommodate such large structures. To optimize the number of configurations to analyse, a genetic algorithm was employed, and a total of 15

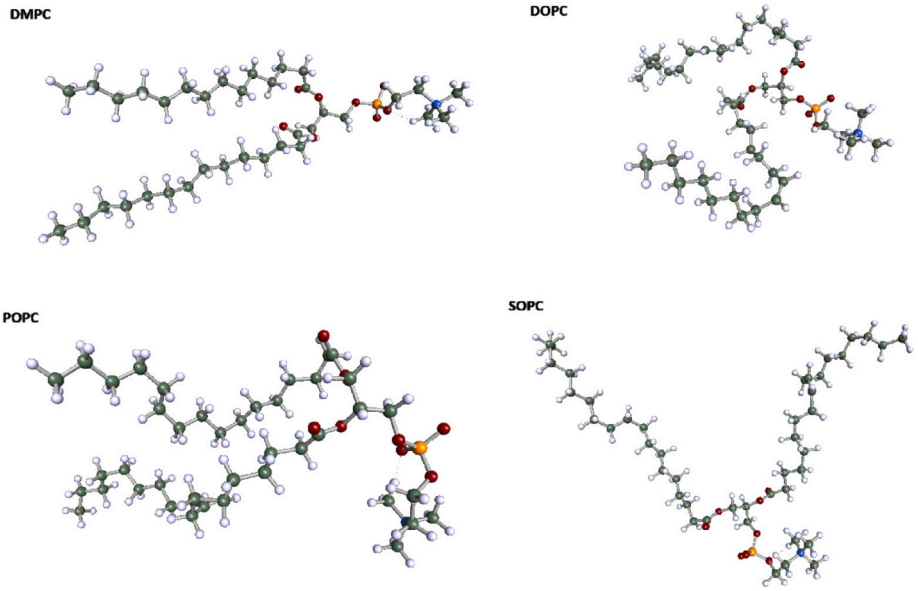

Fig. 1. Structure of all four membrane phospholipids considered on the permeability studies.

poses for each protein/NP combination were calculated. The entire docking procedure was automatized via homemade Python scripts.

2.4. Molecular descriptors

In addition to the results obtained from the membrane and protein interaction studies, a compendium of molecular descriptors was determined for all proteins and NPs -of both MXenes types- from their geometrical structures, to serve as input for the planned predictive models. For the NPs, the library of predictive models from Materials Studio 2024 (BIOVIA, Dassault Systèmes, 2024) was employed. However, due to some software limitations (a hard limit of 1000 atoms or bonds per system for certain descriptors, mainly descriptors based on graph theory in which the atom connectivity and bonds are explicitly needed) the larger size hexagonal Ti_3C_2 NPs are labelled with considerably less descriptors. On the other hand, MOE 2022.02 (Molecular Operating Environment (MOE), 2022) was used for obtaining the protein descriptors at a pH of 7.4, as it is specifically designed for protein analysis and can better handle such a high number of atoms. Nevertheless, a descriptor clean-up was performed for all cases in order to reduce the amount of data to process, based on the variability of the descriptor values themselves. Descriptors that could not be calculated -due to requiring a periodic or electrically charged system, such in the NPs-, those who had the same value for all systems -like the calculation pH of the proteins, or the number of organic functional groups in NPs- or those who had overall few data -such as the number of chiral centres in NPs, which can be difficult to determine- were removed. This clean-up and removal were substantially more needed for the MXene NPs than for the proteins, for which only the pH of calculation was removed.

After clean-up, a total of 21 descriptors were preserved for the proteins, however, two options were considered for the NPs. If all available NPs were included, a total of 33 descriptors would be obtained for each one. Nevertheless, excluding the larger Ti_3C_2 NPs due to the imposed hard limits of the software, that number significantly rose to 80, resulting in two different sets that would be tested. The combination of the number of systems and descriptors yields a total of 5643 data entries (4849 using more NPs but less descriptors) that would serve as the response variable, and 101 (or 54 for all NPs) descriptors as independent variables. Two lists containing all NPs and protein descriptors can be found in the Supporting Information, in an Excel spreadsheet called *Descriptors.xlsx*.

2.5. Predictive model development

Lastly, the development of ML based predictive models was performed with MATLAB R2024A employing its Statistics Machine Learning module (The MathWorks Inc, 2024a; The MathWorks Inc, 2024b), which provides efficient tools designed for the analysis of large amounts of data and a vast list of models of various types for training and fitting. Due to their nature, however, ~~such~~ a large amount of data is often needed for the creation of a proper model. In this work, while the permeability studies provided abundant data, the analysis was limited, comprising the behaviour of a reduced number of small NPs in four similar membranes, hence the resulting model would not be representative enough of the expected trends. The protein docking data set, on the other hand, possessed all materials, shapes and sizes, as well as proteins of very different shapes and functions, and consequently was more suitable for the development of predictive models.

Within the MATLAB environment and its statistical analysis tools, the 25% of the total data was discarded for testing a common value in data science to get a sizeable number of samples for testing-; therefore, the model itself was developed with the remaining ones. As for the model, all ML options implemented in MATLAB were tested: regressions, decision trees, supporting vector machines, neural networks, etc. The application, or not, of a Principal Component Analysis (PCA) was also tested, and several parameters such as the coefficient of determination, R^2, served as quality measurements.

3. Results and discussion

3.1. Nanoparticle library

All NPs mentioned in the last section -that is, three shapes of ten sizes each for each of the two MXenes selected-, were successfully optimized with the only exception of the H10 one, because of their large number of atoms supposed a high computational cost. Nevertheless, the already available NPs of that shape and similar size were considered more than enough. Some representatives can be seen in Fig. 2; note that the H10 shown is not an optimized structure and is included just for visualization purposes.

Regarding the geometries, noticeable distortions relative to the original perfect structure were observed, as expected. These deformations are more pronounced for the smaller NPs, which tended to

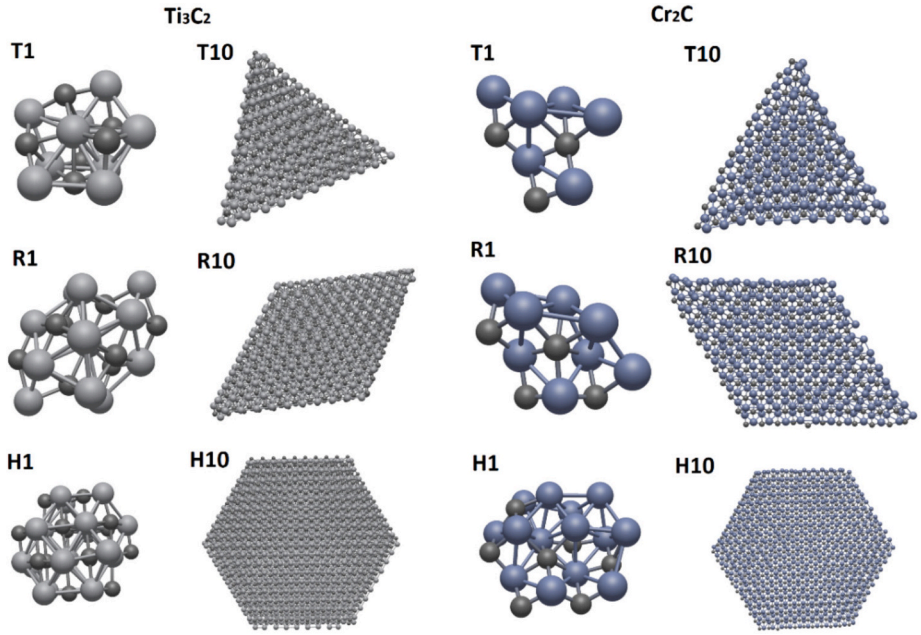

Fig. 2. Examples of several optimized MXene NPs in all shapes and limit sizes. The shapes represented are T (triangular), R (rhombic), and H (hexagonal), with sizes 1 and 10 corresponding to the smallest and largest NPs (top to bottom), respectively, for each shape of Ti_3C_2 (left) and Cr_2C (right).

rearrange and crumble into quasi spherical clusters, making the original shape difficult to discern. As the NPs size increases, the defects became more confined to the edges and corners but, in overall, the general shape of the NPs is maintained and recognizable. In the case of the Cr_2C NPs, an additional deformation is observed: the bending of the NP itself, more noticeable for larger systems. The reduction of their cross-section as a consequence of the fewer number of atomic layers in the Cr_2C crystalline precursor, results in a less constrained structure that is more susceptible to out-of-plane deformations. A similar effect could occur for the Ti_3C_2 NPs as well, but the resulting bending would be much less pronounced, as no noticeable deformation of this type was observed.

Afterwards, with the aim of investigating which morphologies are the most stable for the range of sizes considered in this work (0.5–6 nm of diameter), we investigated the evolution of the $(Ti_3C_2)_n$ and $(Cr_2C)_n$ NPs relative stability when increasing their size (i.e. the number of units (n)) for their different shapes, as it is represented in Fig. 3. Notably, whereas for small size Ti_3C_2 NPs hexagonal remains the most stable shape, upon reaching a certain unit threshold (n ~ 80), triangular and rhombic NPs become more stable. However, when moving to the bulk behaviour (n → ∞) hexagonal NPs are about 3.7 and 3.5 eV/unit more stable with respect to rhombic and triangular particles (see Table S2), respectively. In the case of Cr_2C NPs, the differences between shapes are less pronounced, being the hexagonal one the most stable most of sizes considered here. Nonetheless, upon reaching a number of units about n ~ 340, rhombic NPs turn out more stable, and in the bulk-like behaviour, they are about 2.5 and 1.4 eV/unit more stable when compared with the hexagonal and triangular ones, respectively (see Table S2).

Unfortunately, due to both, the high computational cost derived from computing the electrostatic potential for such large nanoscale systems, and the internal issues of COSMOTherm to estimate the profile of systems with certain electronegativity differences; only a small set of NPs was included in the COSMO analysis. This set of NPs used for the membrane interaction studies is collected in Table 1, with their respective σ-profiles compiled in the Supporting Information and seen in a compound plot on Fig. 4 alongside the phospholipid profiles. As can be seen there, many of the NPs studied have a high distribution around zero surface charge, something visible for both MXenes but with a few cases (R2 and T3 for the Cr_2C) in which the distribution is very spread.

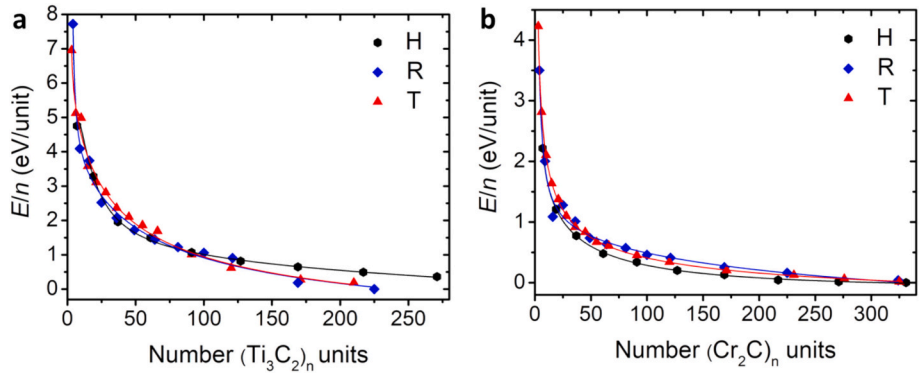

Fig. 3. Relative ground state energies per chemical unit as function of the number (n) of a) $(Ti_3C_2)_n$ and b) $(Cr_2C)_n$ units for the hexagonal (H), rhombic (R) and triangular (T) NPs. The energy of the most stable NP of each series has been set as zero reference. We used the Spherical Cluster Approximation (SCA) (Johnston, 2002) for fitting the curves by following the fourth order expression: $E(n) = a_0 + a_1{*}n^{-1/3} + a_2{*}n^{-2/3} + a_3{*}n^{-3/3} + a_4{*}n^{-4/3}$. All fitting coefficients are reported in Table S2.

Table 1
NP size ranges available for permeability studies for each MXene and shape combination.

MXene	Shape		
	Triangular	Rhombic	Hexagonal
Ti_3C_2	1–7	1–5	1–2
Cr_2C	1–4	1–2	1

3.2. Permeability results

3.2.1. Solute distribution

3.2.1.1. Ti_3C_2 MXene nanoparticles. The plots of the solute distribution for all Ti_3C_2 NPs can be seen in Fig. 5. Due to the large amount of data, each plot displays temperature dependence via a colour scale ranging from blue (low temperature) to red (high temperature), and only the DMPC membrane cases are shown in the manuscript; for a full comparative view, the original images of the plots for all membranes and NPs combinations can be found in the Supporting Information (*Ti3C2 Distributions.png*).

From a general point of view, all solute distribution plots show that, regardless of the membrane type, NP size or shape, and temperature, none of the considered NPs are able to permeate the membrane, as the solute distribution at depth 0 -the membrane centre- is essentially null for all cases. Nevertheless, the NPs accumulate on the membrane surface, interacting more effectively with the polar head groups of the phospholipids. The maximum depth reached varies from case to case, but as a general rule, no NP reaches greater depths than 14 Å, around halfway of the phospholipid length. In some of them, the presence of sharp distribution peaks at specific distances indicates the existence of a preferred penetration depth instead of a smooth continuous distribution.

The main consideration is the apparent lack of any effect associated to the membrane composition -see the forementioned grid of plots in the SI-. Comparing the solute distributions across all membranes, very little difference can be observed between DMPC, SOPC and POPC, while DOPC shows appreciable discrepancies, often manifesting as additional probability secondary peaks or a distortion of the general distribution structure. This different behaviour can be explained in terms of the different ~~geometrical conformation~~ chemical nature of the DOPC molecule with respect to the others: while DMPC, SOPC and POPC have all at least one fully saturated fatty acid chain, in DOPC both chains have a double bond in a cis configuration, which results in a less efficient packing as the long apolar chains are fixed in a bent shape and cannot align so closely, and the number of van der Waals interaction between them decreases. This leaves a less compact membrane structure in which solutes can enter more easily.

Regarding the effect of the NP size and shape, the smaller NPs exhibit a smoother behaviour, with the solute distribution varying slowly with temperature, without detecting appreciable steep jumps between curves. In addition, a common behaviour is observed, as all curves intersect at a particular depth, regardless of the temperature. In these cases, higher temperatures enable the NPs to reach higher depths within the membrane, suggesting a more ideal diffusive behaviour. For larger NPs, on the other hand, this trend disappears; the smooth variation gets disturbed with sharp peaks and plateaus, for some, even occupying the whole plot. There is no clear trend relatable to the actual magnitude of the peaks, but it is noticeable that the temperature effect is inverted: at higher temperatures, the NPs tend to accumulate on outer layers, observing steep jumps between curves and a more erratic behaviour, discarding any sorts of diffusive behaviour; instead, the accumulation of oxygen atoms from the phospholipids near the membrane surface (the polar residue) and the hydrophilicity and high affinity for oxygen of the titanium suggests a consistent deposition with little penetration, consistent with the experimental observations (Nawaz et al., 2025).

3.2.1.2. Cr_2C MXene nanoparticles. In a similar fashion, distribution plots for Cr_2C NPs within the DMPC membrane are shown in Fig. 6, with the same colour coding and axis meaning, with the full compound image in the Supporting Info (*Cr2C Distributions.png*). Compared to the Ti_3C_2 cases, however, the Cr_2C behaviour is considerably less variable, exhibiting only two remarkable tendencies: the most common case, a well localized and narrow distribution near the 22–24 Å, with barely any temperature dependence or additional features except for a small peak located at a more external layer for the H1 NP, and in some isolated cases, a smooth yet small displacement of the peak of this distribution with temperature, as in T2 for DOPC or T1 in SOPC.

In this case, the differences between membranes are minimal, even with the DOPC, that showed noticeable discrepancies in the interaction observed with Ti_3C_2 MXene NPs, suggesting that the geometrical differences between the membrane phospholipids have a negligible effect on the Cr_2C NPs behaviour, which could be associated to the smaller size of this type of NPs. While some extra features arise on certain membranes, like the secondary peak forementioned, there is not enough consistency to attribute it to the membrane composition rather than to the peculiarity of the NPs.

Lastly, despite the electrostatic potential of certain NPs (R2 and T3) was successfully computed, it was not possible to analyse their interaction with the membranes as the obtained results, as they yielded fully null solute distribution plots and extreme values for many properties. This is most likely due to the peculiarity of their corresponding *cosmo* files, which show very steep changes on the surface charge across the system; in many cases the software itself fails to carry out a calculation and freezes or crashes upon trying it; in others, like these two cases, it manages to end, but the results are not representative of the nanoparticle behaviour, and this have been excluded from the results section. It is remarkable that these specific NPs are also the ones that deviated from the rest and had a much more spread σ-profile than the rest; their anomalous behaviour can be tied to the calculated σ-surface, although the exact origin a bad electronic convergence, or a faulty generation of the surface, etc- is not clear, nor can be elucidated with only two cases.

3.2.2. Permeability and partition

While the solute distribution provides information about the membrane on a localized basis, other values such as the permeability and the partition coefficient represent the membrane behaviour as a whole, thus supplying results that can be more usable in a broader toxicological context. For example, the permeability, log(Perm), gives an insight on the speed of the interaction process, as it represents how fast the solute travels through the membrane, being therefore a parameter that allows quantification of the speed of the toxicity mechanism itself. The partition coefficient, $\log(K_{OW})$, on the other hand, shows in which extent the solute remains within the membrane, which correlates with the bioaccumulation potential of the solute and its long-term toxicity effects. Both parameters are presented for the DMPC membrane and NPs combination as a function of the temperature in Fig. 7, while the full plot figures can be found in the Supplementary Information (files *Partition coefficients.png* and *Permeabilities.png*)

3.2.2.1. Permeability. The analysis of the obtained plots reveals that there are few general remarks that can be highlighted. First, it can be concluded that the permeability is excruciatingly slow for all membranes, NPs and temperatures, although a certain increase can be observed in the latter case for a few systems. The permeability for Cr_2C NPs is higher by a few orders of magnitude, but it is still very low to induce any membrane movement.

For Ti_3C_2 NPs, the most common trend is a sawtooth-shaped plot that hints a erratic movement conducted in sudden bursts rather than a continuous and diffusive one, which is the case of the smaller cases such as T1, T2 and the high temperature portion of the small NPs for rhombic and hexagonal shape. T6 also displays a continuous trend, although in a

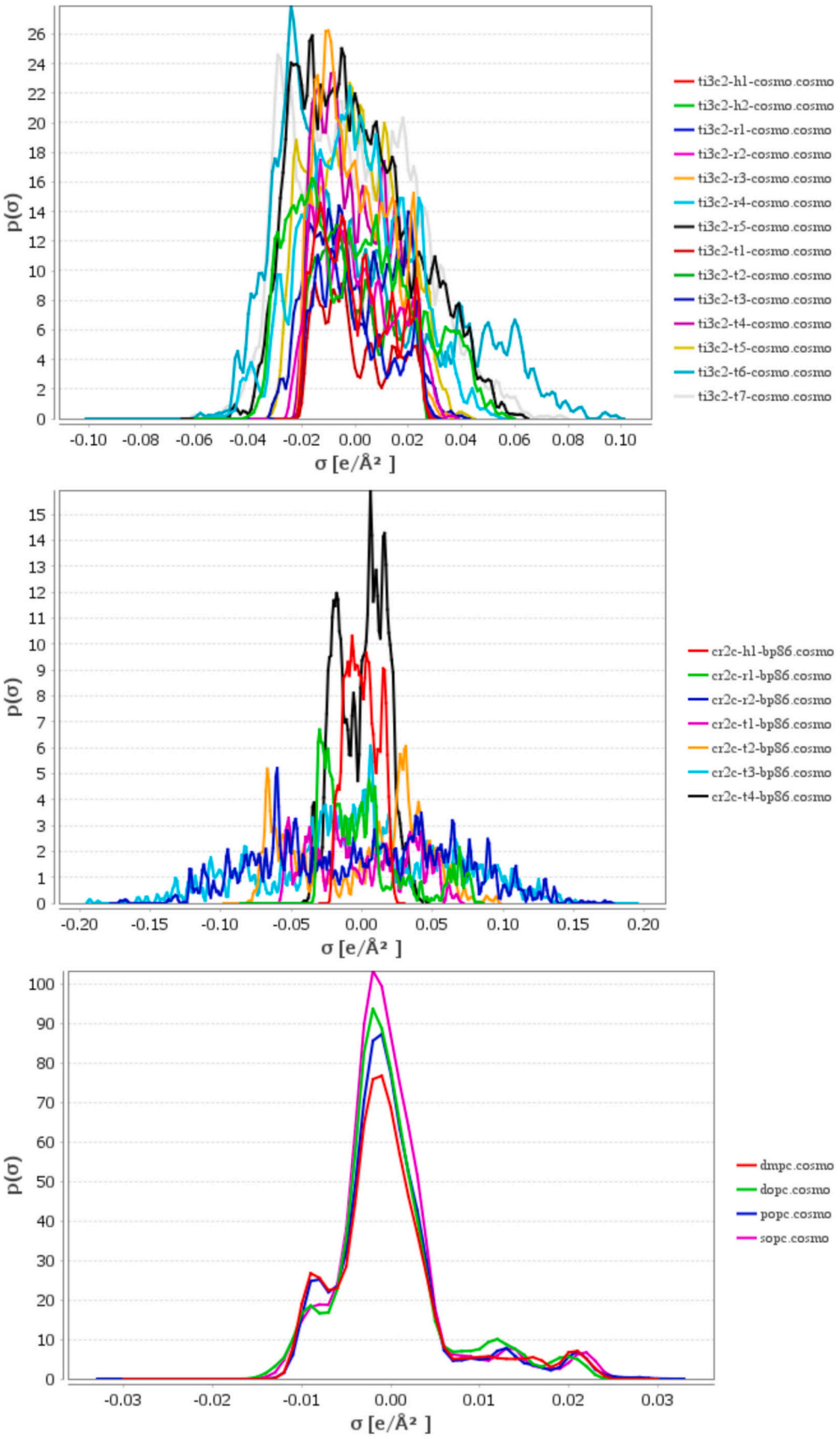

Fig. 4. Compound σ-profile plots for the Ti_3C_2 NPs (top), Cr_2C NPs (middle) and membrane phospholipids (bottom) used in this study.

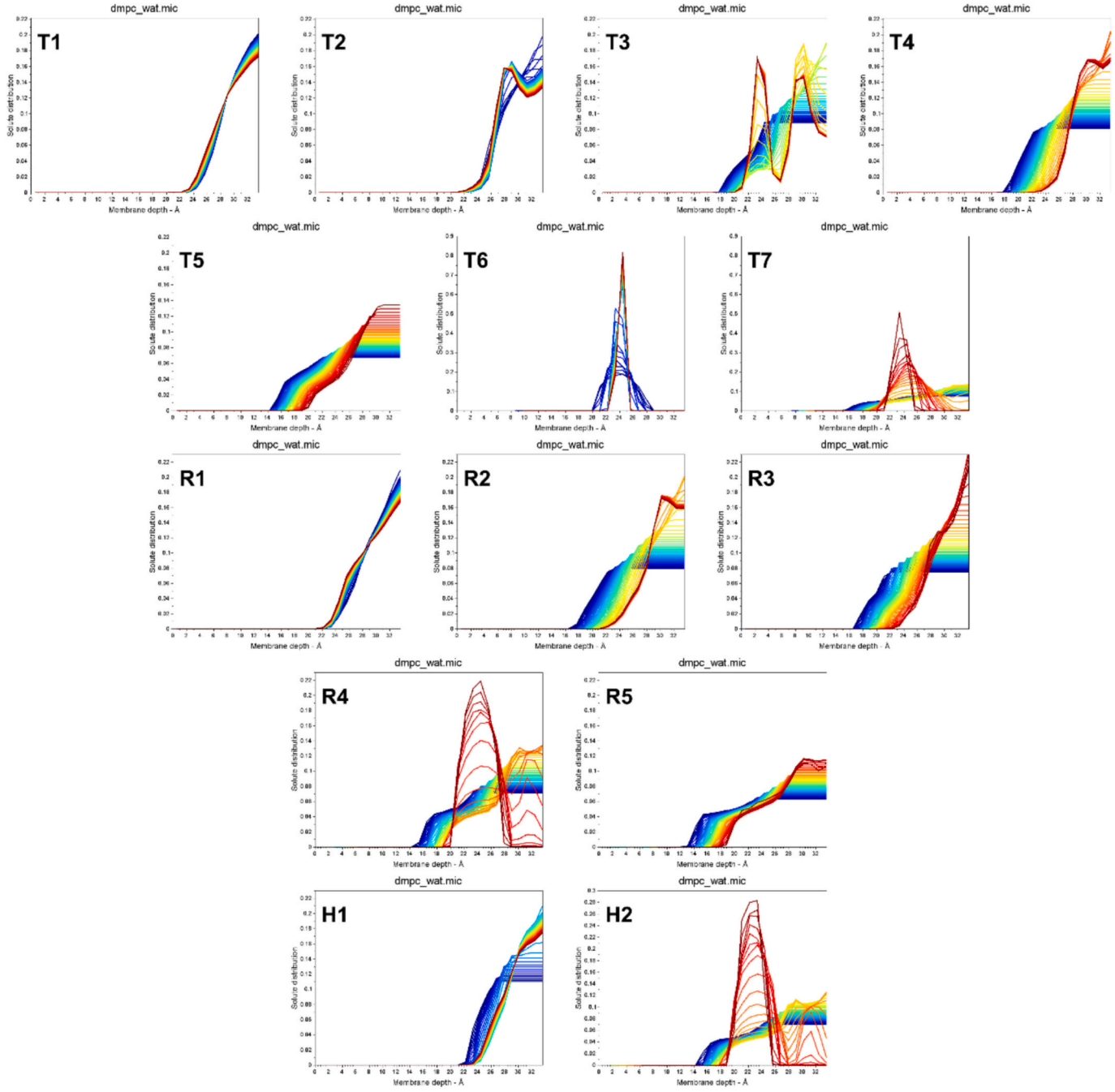

Fig. 5. Solute distribution plots for all tested Ti_3C_2 NPs of Triangular (T), Rhombic (R) and Hexagonal (H) shape, arranged by size (T1 to T4, R1 to R2 and H1, top to bottom) on a DMPC membrane. Colour scale: blue (0 °C) to red (50 °C). (For interpretation of the references to colour in this figure legend, the reader is referred to the web version of this article.)

much lower value that matches its anchoring at a given depth within the membrane.

Cr_2C NPs show a much more regular behaviour, with only a few jumps in a sporadic fashion. Overall, the permeabilities are orders of magnitude higher than for Ti_3C_2, but still very low. There is very little effect of temperature as most of them tend to wedge inside the membrane, with the exception of H1, that follows a more diffusive behaviour, and R1, with a slow decrease. A subtle descent is also observed for larger Ti_3C_2 NPs, matching the higher accumulation at the surface for higher temperatures, but it is still a minor effect.

In a final stage, the effect of the specific type of membrane employed in permeability is not evident. Some differences can be observed for DOPC, as before, which are clearer for the Cr_2C MXene NPs, such as the vast change on permeability for the R1 NP, or the decreasing permeability for the T6 in Ti_3C_2, but besides these outliers, no clear nor consistent modifications can be appreciated between membranes, yielding to a similar behaviour which is much more influenced by the inherent nature of the NPs.

3.2.2.2. Partition coefficient. The partition coefficient plots show a clearer picture of the penetration behaviour already observed, highlighting the persistence of the MXene NPs within the membrane, which is commonly recognized in the Cr_2C case, and occasionally observed in the Ti_3C_2. For Ti_3C_2 most NPs exhibit negative values of $\log(K_{OW})$, which implies a higher solubility in aqueous media than in lipid-like ones because of their known strong hydrophilic character, which translates

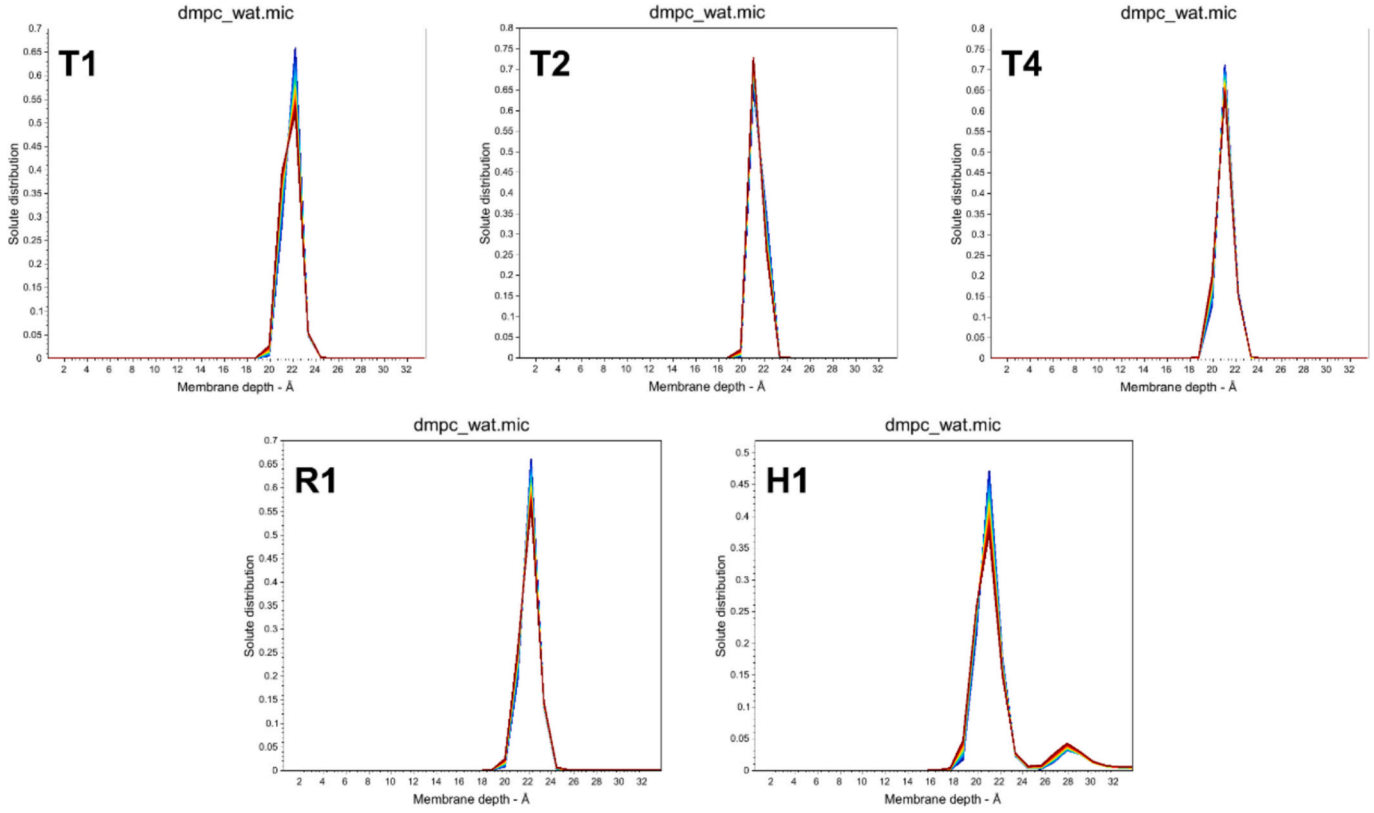

Fig. 6. Solute distribution plots for all tested Cr_2C NPs of Triangular (T), Rhombic (R) and Hexagonal (H) shape, arranged by size (T1 to T4, R1 to R2 and H1, top to bottom) on a DMPC membrane. Colour scale: blue (0 °C) to red (50 °C). (For interpretation of the references to colour in this figure legend, the reader is referred to the web version of this article.)

into a low bioaccumulation risk. This property remains fairly constant with temperature except for a few cases, such as T7, R4 and H2, whose log(K_{OW}) increases beyond a specific temperature, around 35 °C–37 °C in general, reaching values of up 15, indicative of a very high potential of bioaccumulation. The T6 case is a clear exception, with values that easily dwarf the rest of NPs and that match its tendency to stay wedged inside the membrane, as observed earlier.

Cr_2C NPs, with their similar trends and distributions already showcasing high accumulation, display positive partition coefficients all across the board, reaching values as high as of 20 and hinting at a high affinity for hydrophobic environments. A slight decrease with temperature can be observed, as well as larger values overall for the DOPC case, but it is evident the bioaccumulation that these systems pose, regardless of temperature, size and shape.

It is important to interpret these extreme log(K_{OW}) values with appropriate caution. COSMO-RS partition coefficients are known to be less reliable for very large, anisotropic solutes such as 2D nanoparticles ~~flakes~~, in part because the method assumes quasi-spherical solvation shells and does not fully capture membrane deformation, lateral compression, or curvature effects induced by extended planar surfaces. In addition, optimized MXene NPs tend to flatten or align parallel to the membrane interface, which can artificially increase the calculated interfacial stabilization and therefore inflate the predicted lipophilicity. These factors imply that the highest log(K_{OW}) values reported here should be considered as upper-bound estimates rather than strict quantitative predictions, indicating a *possible* bioaccumulation tendency rather than a confirmed toxicological mechanism. Since these breakpoint temperatures are within the normal range for a human body, these results show a high toxicological hazard on regular physiological conditions.

3.3. Proteins docking results

From the docking calculations performed, the main outputs from the docking calculations are the binding energies of the most stable configuration, which in most cases, but not necessarily, is also the most common situation, and give information about the most realistic scenario in an actual protein-NP interaction. Given the large number of combinations, it is not feasible to present all the obtained values in a concise and visual manner. Instead, in this study the results are presented as the heatmap matrix displayed in Fig. 8, with the colour showcasing the relative binding energies. The actual values can be found in the Supporting Information, on a dedicated Excel spreadsheet called *Docking Results.xlsx*. Note that the proteins were named following the RCSB Protein Data Bank (RCSB PDB), which serves as the primary source of structural data for AutoDock simulations.

The heatmap colour code is as follows: red indicates the strongest bindings (more negative binding energy values), green the weakest bindings (less negative or even positive values) and yellow for the intermediate cases. The red colour tone is capped at −2 eV to avoid spurious values shifting artificially the heatmap.

A few considerations may be taken into account: first, the protein 4fr8 (aldehyde dehydrogenase-2) had no data due to its size, surpassing the hardcoded limit of atoms imposed by Autodock, at around 32,000. Autodock Vina could surpass it, but the easiness of parametrization of Autodock was needed for this study.

Secondly, the Cr_2C H8 NP shows very strong binding energies, with values between −8 and − 11 eV, for all proteins, a huge difference from the rest of the NPs studied regardless of material, shape or size. This NP was generated the same way as the others, and repeated docking runs yielded the same results, so computational noise or file issues are discarded as the reason. Given its isolated nature, this behaviour is best interpreted as a methodological artifact inherent to the rigid-body

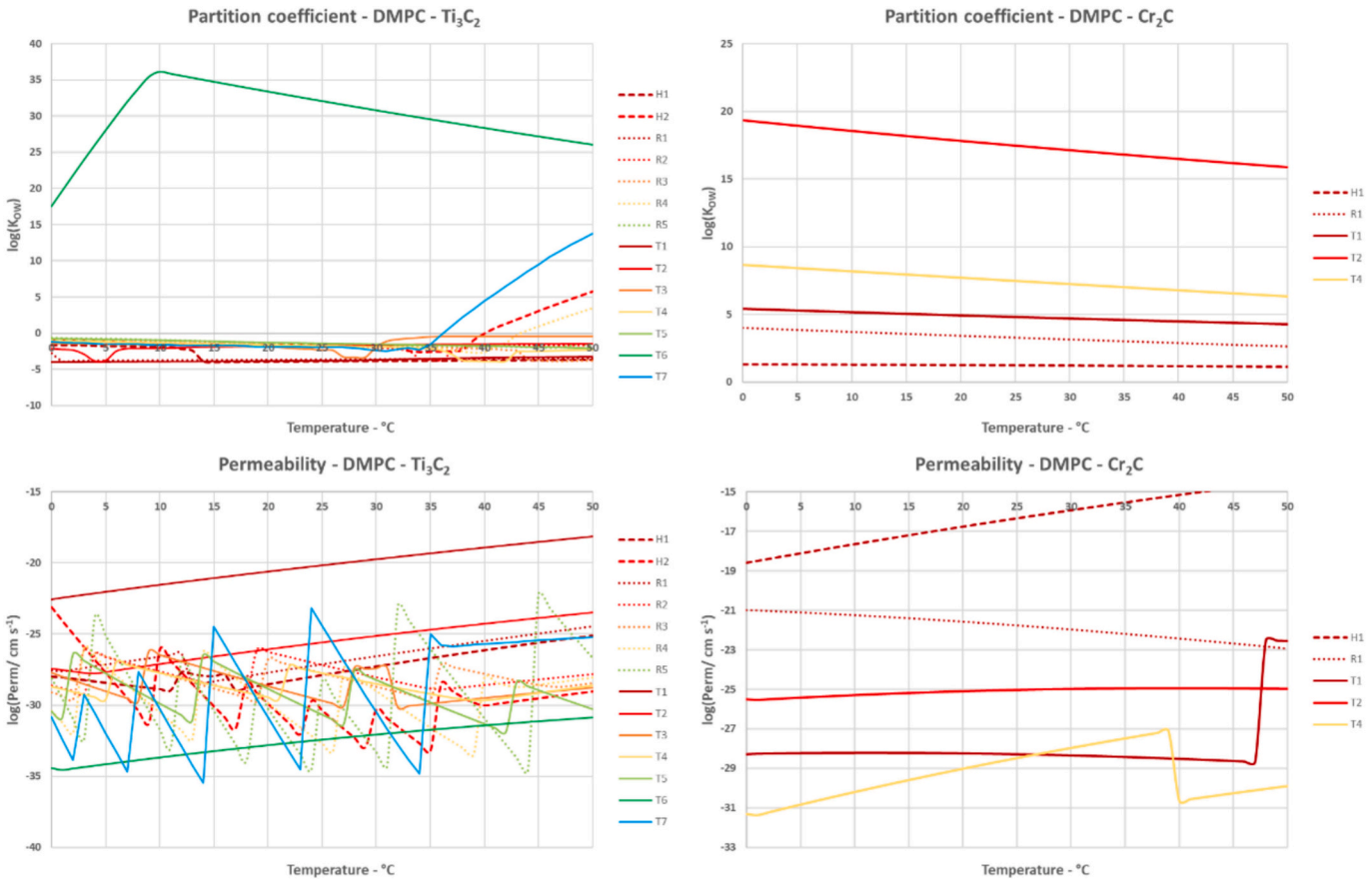

Fig. 7. Permeability plots for both MXenes and all four membrane combinations, as a function of temperature.

docking approximation itself, which can overestimate surface interactions for large, flat NPs such as this one, and are not directly comparable to the remaining systems. Due to this, and to avoid introducing model bias, the results corresponding to this NP were excluded from the subsequent data analysis.

Focusing on the bulk of the data, the results indicate that there is a net, attractive interaction for all protein-NPs couples, with values commonly between −0.1 to −1.5 eV, which would situate them more in line with electrostatic interactions rather than fully chemical bonds. Observations of the final disposition for a few randomized NP-protein pairs (Fig. 9) shows that the NPs tend to stay on the outer protein surface for both large and small NPs even though the latter would not have any issues reaching inner cavities. Combined with the weak energies, this concludes that the protein-NP interaction is similar to a corona formation phenomenon, with the MXene surrounding it in a role reversal situation. It is expected for these shell structures to be labile and fragile, with small consequences to the protein activity.

Regarding more specific factors, the material itself tends to have a marked effect, with Cr_2C showing more yellow and red tones on the heatmap in contrast to the greens of Ti_3C_2. The values for Cr_2C are commonly 0.5 to 1 eV higher in absolute value, with matches the more expected interaction and potential toxicity for Cr_2C than for Ti_3C_2. However, a mildly stronger surface binding does not constitute by itself a proof of toxicity, just a requirement for it.

The shape of the NPs also seems to have an effect on the binding energy, although milder than the material. Both materials appear to follow a Hexagonal > Rhombic > Triangular order, more pronounced on the Cr_2C MXene, and with a few exceptions on R3 and R6 for Cr_2C, showing remarkably weaker interactions. Given the structural deformations the NPs experienced upon optimization, there are many structural factors at play; however, the most straightforward explanation is the higher number of metallic surface atoms, which also follow the Hexagonal > Rhombic > Triangular order, thus obtaining a stronger interaction.

As for the size, it is noticeable how the binding energy tends to decrease as the size of the NP does, and the heatmap shifting to a more yellow/green colour as a consequence, specially on the Ti_3C_2. The explanation is also easy to deduce: the NPs keep an overall flat shape as they grow, so even if they do have more atoms to interact with, the relative contact surface with the protein is low. Also, they find increasing difficulties to enter any cavities or holes as they grow in size as well. However, the docking approach used considers the NPs as total rigid structures, and the flexibility of the material may change this outcome, should it be considered in the future.

Lastly, there is little discernible effect of the protein on the binding energy, as no specific proteins nor families display a remarkably higher affinity for the MXene NPs in any combination. There are some similar behaviours within the cytokine and membrane protein families, as well as some rogue cases with either stronger interactions that average, such as 1p0p (butyryl cholinesterase) and 1yk8 (cathepsin K), or even lower for the 2kax metal binding protein, but no significant trends can be extracted in any case. Instead, this mass docking can serve as a first glace for future work and higher cost computational efforts.

3.4. *Predictive models*

As a conclusive effort to extract more than a simple qualitative overall trend compilation from all the data obtained so far, its use for the development of ML based predictive models has been carried out. The goal of this last part is to design a mathematical tool enable to predict the toxicological properties showcased all across the paper, but using molecular descriptors as input in a quicker and simpler fashion, either

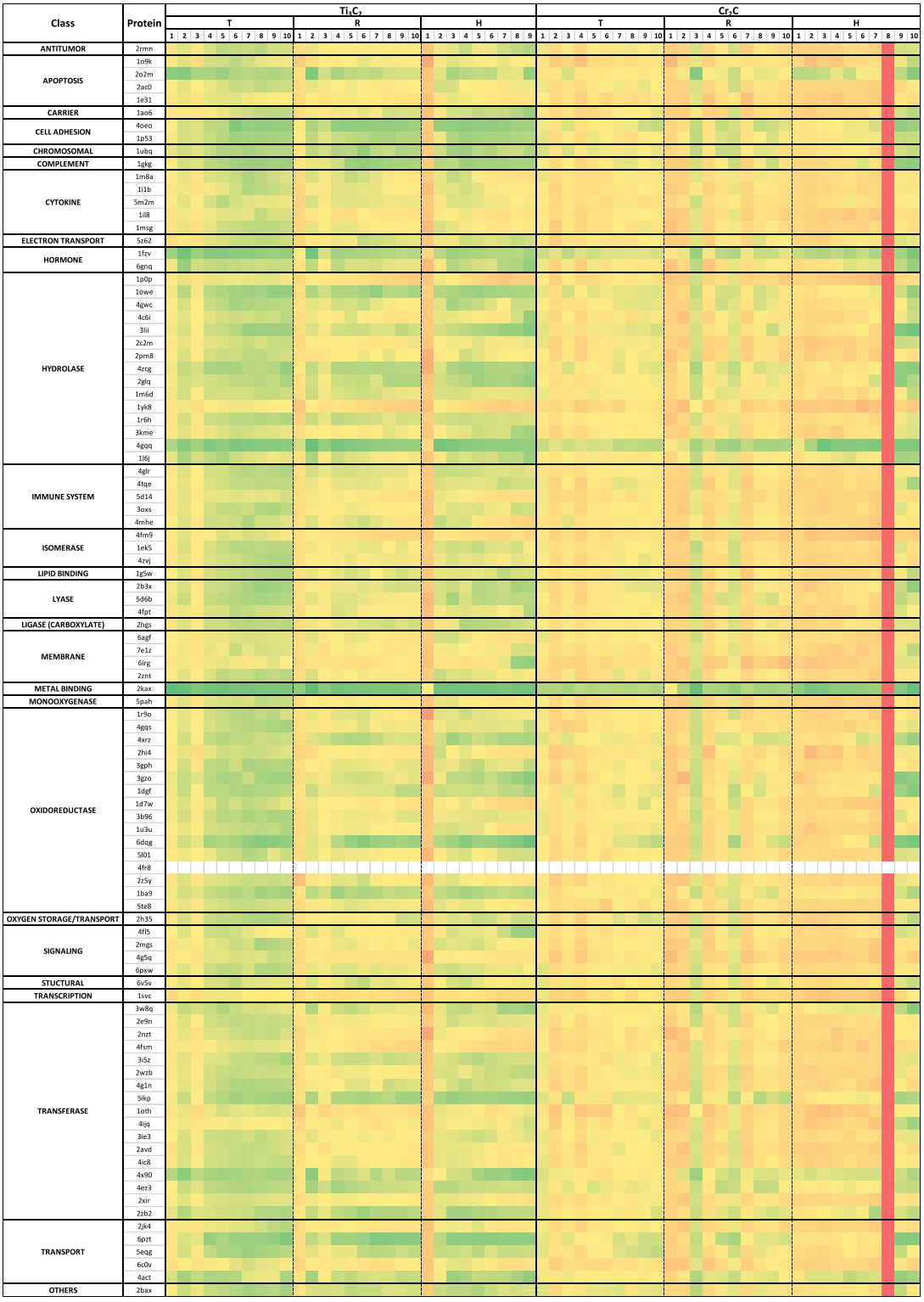

Fig. 8. Coloured heatmap showcasing the relative binding energies for all protein-MXene NPs combinations simulated. Shape legend: T – Triangular; R – Rhombic; H – Hexagonal.

through a concise mathematical expression or a trained predictive model. As mentioned before, only the docking analysis data will be used, due to its larger amount of data available.

The two different training data sets -as explained in section 0- were treated in the same way: the binding energy was treated as response variable, a 25% of the data were randomly selected to act as test data set, and the default 5-fold cross-validation method suggested by MATLAB was selected. For training, all available models offered by MATLAB were tested with their default hyperparameters, including and excluding the PCA analysis for comparative purposes. The model quality was evaluated via the usual parameters: RMSE and R^2 for both test and training sets, as can be seen in Table 2.

For both cases, the best performing model type is the Ensemble of Bagged Trees, a model particularly known for its high accuracy at the

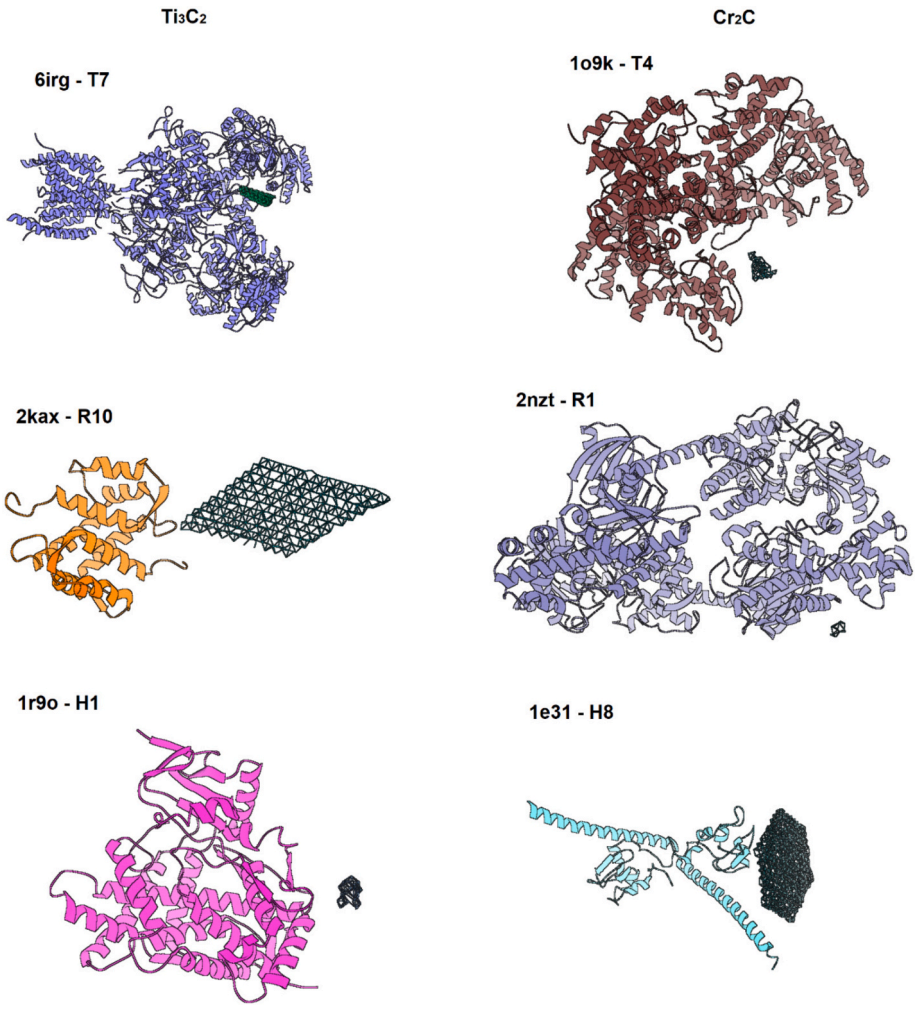

Fig. 9. Examples of the most stable configuration between NPs and protein for several Ti_3C_2 (left) and Cr_2C (right) cases, shown for some of the chosen proteins.

Table 2
Performance parameters of the two Bagged Trees predictive models selected from the training, along the number of factors, NPs and data of each, and the results with a PCA.

Model	# Factors	# NPs	# Data	Validation		Test	
				RMSE	R^2	RMSE	R^2
All NPs	21 + 33	58	5683	0.072	0.833	0.071	0.834
All NPs - PCA				0.122	0.525	0.118	0.540
All Factors	21 + 80	50	4849	0.072	0.831	0.067	0.854
All Factors - PCA				0.111	0.593	0.109	0.612

expense of its low training speed and high memory requirements for large data sets, which was not an issue since the used data set was not too large. The RMSE values are acceptable among the binding energy values, and the high R^2 values for both validation and testing present them as models of high accuracy and robust across different data sets. They both had the same hyperparameters suggested by MATLAB -minimum leaf size of 8, 30 learners, and all factors were included in the model- and could be equally used depending on the available input data. A Principal Components Analysis was also conducted on these models in a re-training; however, the final outcome was considerably worse, as the RMSE increased, and the R^2 went down considerably. As a result, the models that had all the calculated descriptors as factors directly were selected.

To visually showcase the performance of the selected models, Fig. 10 presents several plots: the response plot as a general view of the model precision, as well as the Predicted vs Actual and Residuals plots for the two models. Both plot sets display a remarkable correspondence between the real data and the values provided by the model, with a clear similitude and a balanced residuals distribution, presenting the obtained models as usable predictive tools able to provide results with an extraordinary accuracy.

Due to the nature of the Bagged Trees model, however, it is not possible to present a concise mathematical expression as in a common regression curve: in the process of elaborating the model, several decision trees are averaged, trading readability with performance. Instead, the MATLAB files for the two models are included in the Supporting Information, as provided by the software itself, called *QSPR_Model_All_Factors.mat* and *QSPR_Model_All_NPs.mat* respectively.

4. Comparison with experimental evidence and limitations

Although the present toxicological assessment is entirely computational, the qualitative trends obtained here are strongly consistent with what is currently known from experimental MXene toxicity studies, particularly for Ti_3C_2-based materials. Among the most detailed reports, Boufidis et al. demonstrated that $Ti_3C_2T_x$ NPs maintain **high astrocyte viability**, do not disrupt membrane functionality, and induce only superficial membrane aggregation without loss of cellular activity (Boufidis et al., 2025). These findings align closely with our results showing **low membrane permeability** for all Ti_3C_2 nanoparticles and

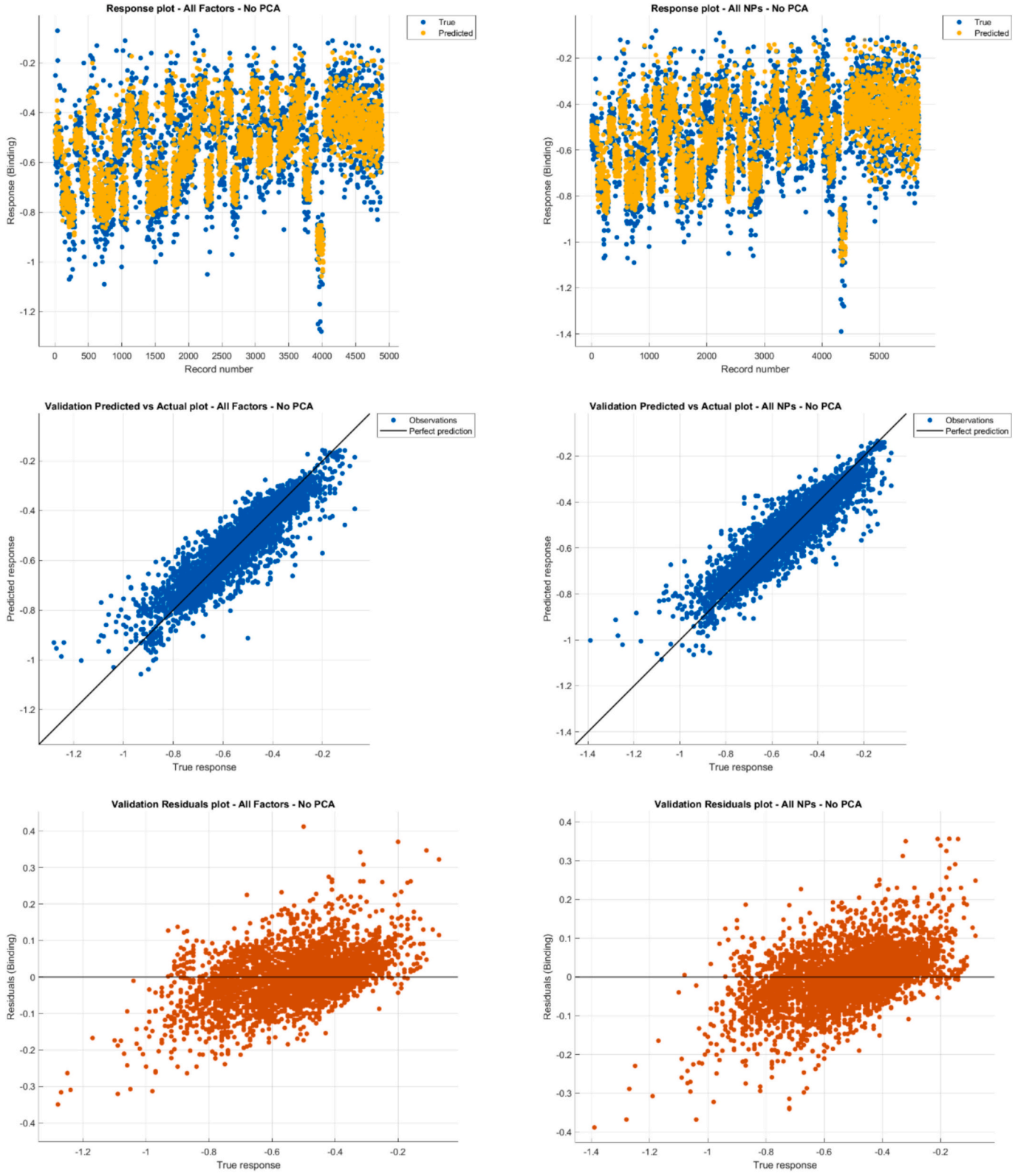

Fig. 10. Performance plots for the two predictive models obtained for the docking studies.

weak, surface-level protein interactions, with binding energies generally between −0.1 and − 0.5 eV across 97 human proteins.

Environmental studies similarly support low intrinsic toxicity for Ti_3C_2. Nawaz et al. observed that Ti_3C_2 exposure in *Scenedesmus quadricauda* resulted in **minimal physiological disruption**, with toxicity being detectable only at elevated concentrations and predominantly linked to shading or surface-coating effects rather than direct molecular damage (Nawaz et al., 2025). This corresponds well with our prediction that Ti_3C_2 NPs largely remain **on the membrane surface**, without penetrating lipid bilayers or accumulating in the hydrophobic core.

More broadly, MXene toxicology studies highlight that Ti-based MXenes tend to be **among the most biocompatible** members of the

family, especially compared with transition-metal MXenes containing more reactive elements (Lim et al., 2021). The reported computational results reproduce this trend: Ti_3C_2 NPs consistently display the **weakest protein binding** across all shapes and sizes, and their predicted partition coefficients suggest **low bioaccumulation potential**, except in a small number of isolated geometries.

In contrast, experimental toxicological data for chromium-containing MXenes are scarce or entirely absent. Nevertheless, it is well established that **chromium-based nanomaterials exhibit greater redox activity** and higher chemical reactivity than their titanium counterparts, a trend widely acknowledged in the nanotoxicology community and reflected in MXene safety analyses. The **moderately stronger binding energies** predicted here for Cr_2C NPs (commonly between −0.5 and − 1.0 eV) are therefore consistent with the expected behaviour of chromium-containing 2D materials. Importantly, however, even in these cases the interactions remain **superficial**, without deep binding or active-site disruption, suggesting that any potential Cr_2C toxicity observed experimentally would more likely arise from **oxidative or dissolution-related mechanisms** rather than direct protein inactivation—an insight that reinforces the mechanistic value of the docking data.

Taken together, the available experimental evidence for Ti_3C_2 MXenes supports the central conclusions of our in-silico study: **poor membrane permeation, limited molecular-level reactivity, weak and non-specific protein binding**, and an overall low intrinsic toxicity under standard biological conditions. At the same time, the computational predictions for Cr_2C highlight important knowledge gaps and motivate **targeted experimental assays** to assess the behaviour of newer MXene chemistries. Thus, our multi-scale modelling framework not only reproduces known experimental trends but also provides predictive guidance for future MXene toxicology research.

Beyond these experimentally consistent trends, it is also important to consider additional toxicity pathways apart of the membrane-association and protein–NP interactions evaluated in this work. One must recognize that MXenes may elicit additional toxicological pathways not directly accessible from the present computational framework. Experimental studies have reported that $Ti_3C_2T_x$ NPs ~~flakes~~ can generate moderate levels of reactive oxygen species under light exposure or in the presence of redox-active biomolecules, potentially contributing to oxidative stress in susceptible cell types (Purbayanto et al., 2022). Similarly, oxidative dissolution or surface degradation—particularly relevant for transition-metal MXenes containing more reactive metals such as chromium—may release ionic species capable of triggering downstream effects including mitochondrial damage, DNA oxidation, or inflammatory signalling. Although such mechanisms were not explicitly modelled here, their absence must be considered when interpreting the relatively benign membrane and protein interaction profiles observed. Instead, the present results should be viewed as defining the subset of toxicity mechanisms *not* strongly supported by molecular-level interactions, thereby helping to isolate ROS-mediated pathways, ion dissolution, immune activation, or genotoxic responses as key experimental priorities for future MXene safety assessments.

5. Conclusions

The multi-approach computation-based toxicological studies carried out in the present work have generated plentiful data to assess the potential hazard mechanisms of MXene Ti_3C_2 and Cr_2C NPs, as well as for demonstrating the applicability and limitations of the computational workflows used.

First, DFT has been proved useful for obtaining realistic MXene NPs as central structures for downstream toxicological analyses, managing to preserve the overall shape and allowing the construction of a sizeable library for all consequent analysis and simulations. Furthermore, these calculations provided a deep insight the most stable morphologies as a function of the NP size, pointing to rhombic and hexagonal Ti_3C_2 and Cr_2C nanomaterials, respectively; as the most likely NPs existing in the few nm scale. It is true that it is not applicable to systems on the range of micrometres, which are usually the sizes commonly seen in the synthesis procedures and measurements, but true NPs can be produced, nevertheless, on an incidental basis, and it is precisely this smaller size what makes them pose a hazard for health, even though the presented systems are idealistic in nature.

The membrane permeability studies showed little to no hazard of the MXene NPs, at least from a simplistic and static point of view, as the NPs tend to stay at the membrane surface and cannot cross it whatsoever, with very low permeabilities and partition coefficients, even though the smaller ones manage to reach deeper. However, some of them show the potential for bioaccumulation and, while being just a few isolated cases, it does constitute a potential toxicological mechanism. Given the model simplicity, further research is needed, with more realistic membranes or considering dynamic methods such as molecular dynamics.

Overall, the docking analysis shows that the interaction between MXene NPs and proteins, while attractive and consistent, is also weak and limited to the outer protein surface, and possibly short lived. No active site interaction has been observed -although it is not feasible to check one by one all cases- and as a result no toxicological effects are expected from this mechanism. However, given the docking calculation simplicity, these results should only serve as a starting point, more suitable for choosing specific cases to work with under more precise and realistic calculations.

Additionally, the copious amounts of results have proven useful for the elaboration, training and testing of several predictive models for a quicker, easier prediction of some of the observed properties. Although only the docking studies and their binding energies have been suitable for this purpose, they had yielded two accurate and robust models that can predict binding energies from simple molecular descriptors from both NPs and proteins.

In conclusion, this in-silico approach demonstrates a viable, efficient methodology for early-stage toxicological assessment of MXene NPs. Several toxicological mechanisms have been tested via multiple and various computational methods, resulting in a low hazard level as shown by the low membrane permeability and weak interaction with proteins, while at the same time hinting at other possibilities such as bioaccumulation, serving as excellent starting point for further, more precise simulations. Overall, these computational insights serve as a strong foundation for guiding more detailed experimental and simulation studies aimed at evaluating the safety of emerging MXene materials. Moreover, the methodology and data presented in this study demonstrate that predictive models help to reduce animal testing of new 2D NPs, such as MXenes, providing new insights into safety assessment within the Safe and Sustainable by Design (SSbD) framework and supporting the development of Integrated Approaches to Testing and Assessment (IATA) guidelines recommended by the European Union.

CRediT authorship contribution statement

Sergio de-la-Huerta-Sainz: Writing – review & editing, Writing – original draft, Visualization, Validation, Methodology, Investigation, Formal analysis, Data curation, Conceptualization. **Valentín Díez-Cabanes:** Writing – review & editing, Writing – original draft, Visualization, Validation, Methodology, Investigation, Formal analysis, Data curation, Conceptualization. **Pedro A. Marcos Villa:** Writing – review & editing, Writing – original draft, Visualization, Validation, Methodology, Investigation, Formal analysis, Data curation, Conceptualization. **Alfredo Bol:** Writing – review & editing, Writing – original draft, Visualization, Validation, Supervision, Methodology, Investigation, Conceptualization. **Laura Gómez-Cuadrado:** Writing – review & editing, Writing – original draft, Validation, Methodology, Investigation, Conceptualization. **Dalia de la Fuente-Vivas:** Writing – review & editing, Writing – original draft, Visualization, Investigation, Data curation, Conceptualization. **Javier Alcodori Ramos:** Writing – review

& editing, Writing – original draft, Validation, Investigation, Conceptualization. **Carla F. Martins:** Writing – review & editing, Writing – original draft, Validation, Investigation, Conceptualization. **Inês T. Meireles:** Writing – review & editing, Writing – original draft, Validation, Investigation, Conceptualization. **Ana Rita Alberto:** Writing – review & editing, Writing – original draft, Validation, Investigation, Conceptualization. **Santiago Aparicio:** Writing – review & editing, Writing – original draft, Validation, Supervision, Software, Resources, Project administration, Methodology, Investigation, Funding acquisition, Formal analysis, Conceptualization.

Declaration of competing interest

The authors whose names are listed immediately below certify that they have NO affiliations with or involvement in any organization or entity with any financial interest (such as honoraria; educational grants; participation in speakers' bureaus; membership, employment, consultancies, stock ownership, or other equity interest; and expert testimony or patent-licensing arrangements), or non-financial interest (such as personal or professional relationships, affiliations, knowledge or beliefs) in the subject matter or materials discussed in this manuscript.

Acknowledgements

Funded by the European Union under GA number 101135965 (SAFARI). Views and options expressed are, however, those of the author(s) only and do not necessarily reflect those of the European Union. Neither the European Union nor the granting authority can be held responsible for them. We also acknowledge SCAYLE (Supercomputación Castilla y León, Spain), CénitS (Centro Extremeño de iNvestigación, Innovación Tecnológica y Supercomputación) for providing supercomputing facilities. Computational resources were also provided by CESGA (CEntro de Supercomputación de GAlicia) supercomputing facilities, under the Red Española de Supercomputacion (RES) grant QHS-2025-2-0025. The statements made herein are solely the responsibility of the authors. Authors declare no competing interests.

Appendix A. Supplementary data

Supplementary data to this article can be found online at https://doi.org/10.1016/j.impact.2026.100624.

Data availability

Data will be made available on request.

References

Aguilar, N., de la Fuente, P., Fernández-Pampín, N., Martel, S., Gómez-Cuadrado, L., Marcos, P.A., Bol, A., Rumbo, C., Aparicio, S., 2025. In silico exploration of graphene nanoflakes: from DFT simulations to machine learning-driven toxicity predictions. NanoImpact 38, 100563. https://doi.org/10.1016/j.impact.2025.100563.

Aleithan, S.H., Ahmad, W., 2025. MXene photodetectors: from materials engineering to versatile optoelectronic applications. Mater. Today Energy 51, 101906. https://doi.org/10.1016/j.mtener.2025.101906.

Anasori, B., Gogotsi, Y., 2023. The global expansion of MXenes. Graphene 2D Mater. 8, 39–41. https://doi.org/10.1007/s41127-023-00067-1.

Balasubramani, S.G., Chen, G.P., Coriani, S., Diedenhofen, M., Frank, M.S., Franzke, Y.J., Furche, F., Grotjahn, R., Harding, M.E., Hättig, C., Hellweg, A., Helmich-Paris, B., Holzer, C., Huniar, U., Kaupp, M., Khah, A.M., Khani, S.K., Müller, T., Mack, F., Nguyen, B.D., Parker, S.M., Perlt, E., Rappoport, D., Reiter, K., Roy, S., Rückert, M., Schmitz, G., Sierka, M., Tapavicza, E., Tew, D.P., Van Wüllen, C., Voora, V.K., Weigend, F., Wodyński, A., Yu, J.M., 2020. TURBOMOLE: modular program suite for ab initio quantum-chemical and condensed-matter simulations. J. Chem. Phys. 152, 184107. https://doi.org/10.1063/5.0004635/16685297/184107_1_ACCEPTED_MANUSCRIPT.PDF.

BIOVIA COSMOtherm, 2026.

BIOVIA, Dassault Systèmes, 2024. BIOVIA Materials Studio, Release 2024.

Boota, M., Anasori, B., Voigt, C., Zhao, M., Barsoum, M.W., Gogotsi, Y., 2016. Pseudocapacitive electrodes produced by oxidant-free polymerization of pyrrole between the layers of 2D titanium carbide (MXene). Adv. Mater. 28, 1517–1522. https://doi.org/10.1002/adma.201504705.

Boufidis, D., Krizman, E.N., Smith, C.M., Xie, Y., Garg, R., O'Donnell, J.C., Vitale, F., Cullen, D.K., 2025. Astrocyte interactions with Ti3C2Tx MXene flakes: insights into viability, morphology, and functionality. Adv. Mater. Interfaces 12. https://doi.org/10.1002/admi.202500261.

Britannica Editors, 2006. Fermi level [WWW Document]. Encyclopedia Britannica. https://www.britannica.com/science/Fermi-level. accessed 12.11.25.

Diez-Cabanes, V., Pastore, M., 2021. Morphological engineering of inorganic semiconductor VIS-light-driven nanocatalysts: experimental and theoretical understandings. J. Phys. Chem. C 125, 15125–15133. https://doi.org/10.1021/acs.jpcc.1c04487.

Diez-Cabanes, V., Morales-García, Á., Illas, F., Pastore, M., 2021. Understanding the structural and electronic properties of photoactive tungsten oxide nanoparticles from density functional theory and GW approaches. J. Chem. Theory Comput. 17, 3462–3470. https://doi.org/10.1021/acs.jctc.1c00293.

Dijkstra, B.W., Drenth, J., Kalk, K.H., Vandermaelen, P.J., 1978. Three-dimensional structure and disulfide bond connections in bovine pancreatic phospholipase a2. J. Mol. Biol. 124, 53–60. https://doi.org/10.1016/0022-2836(78)90146-8.

Draško Tomić, 2024. The Vini In Silico Model for Cancer [WWW Document]. https://github.com/draskot/Vini accessed 3.10.26.

Eckert, F., Klamt, A., 2002. Fast solvent screening via quantum chemistry: COSMO-RS approach. AICHE J. 48, 369–385. https://doi.org/10.1002/aic.690480220.

Frisch, M.J., Trucks, G.W., Schlegel, H.B., Scuseria, G.E., Robb, M.A., Cheeseman, J.R., Scalmani, G., Barone, V., Petersson, G.A., Nakatsuji, H., Li, X., Caricato, M., Marenich, A.V., Bloino, J., Janesko, B.G., Gomperts, R., Mennucci, B., Hratchian, H. P., Ortiz, J.V., Izmaylov, A.F., Sonnenberg, J.L., Williams-Young, D., Ding, F., Lipparini, F., Egidi, F., Goings, J., Peng, B., Petrone, A., Henderson, T., Ranasinghe, D., Zakrzewski, V.G., Gao, J., Rega, N., Zheng, G., Liang, W., Hada, M., Ehara, M., Toyota, K., Fukuda, R., Hasegawa, J., Ishida, M., Nakajima, T., Honda, Y., Kitao, O., Nakai, H., Vreven, T., Throssell, K., Montgomery, Jr.J.A., Peralta, J.E., Ogliaro, F., Bearpark, M.J., Heyd, J.J., Brothers, E.N., Kudin, K.N., Staroverov, V.N., Keith, T.A., Kobayashi, R., Normand, J., Raghavachari, K., Rendell, A.P., Burant, J. C., Iyengar, S.S., Tomasi, J., Cossi, M., Millam, J.M., Klene, M., Adamo, C., Cammi, R., Ochterski, J.W., Martin, R.L., Morokuma, K., Farkas, O., Foresman, J.B., Fox, D.J., 2016. Gaussian 16 Revision C.01.

Ghidiu, M., Lukatskaya, M.R., Zhao, M.-Q., Gogotsi, Y., Barsoum, M.W., 2014. Conductive two-dimensional titanium carbide 'clay' with high volumetric capacitance. Nature 516, 78–81. https://doi.org/10.1038/nature13970.

Goedecker, S., Teter, M., Hutter, J., 1996. Separable dual-space gaussian pseudopotentials. Phys. Rev. B 54, 1703–1710. https://doi.org/10.1103/PhysRevB.54.1703.

Grimme, S., Antony, J., Ehrlich, S., Krieg, H., 2010. A consistent and accurate *ab initio* parametrization of density functional dispersion correction (DFT-D) for the 94 elements H-Pu. J. Chem. Phys. 132. https://doi.org/10.1063/1.3382344.

Hjorth Larsen, A., Jørgen Mortensen, J., Blomqvist, J., Castelli, I.E., Christensen, R., Dułak, M., Friis, J., Groves, M.N., Hammer, B., Hargus, C., Hermes, E.D., Jennings, P. C., Bjerre Jensen, P., Kermode, J., Kitchin, J.R., Leonhard Kolsbjerg, E., Kubal, J., Kaasbjerg, K., Lysgaard, S., Bergmann Maronsson, J., Maxson, T., Olsen, T., Pastewka, L., Peterson, A., Rostgaard, C., Schiøtz, J., Schütt, O., Strange, M., Thygesen, K.S., Vegge, T., Vilhelmsen, L., Walter, M., Zeng, Z., Jacobsen, K.W., 2017. The atomic simulation environment—a python library for working with atoms. J. Phys. Condens. Matter 29, 273002. https://doi.org/10.1088/1361-648X/aa680e.

Hutter, J., Iannuzzi, M., Schiffmann, F., VandeVondele, J., 2014. <scp>cp2k: </scp> atomistic simulations of condensed matter systems. WIREs Comput. Mol. Sci. 4, 15–25. https://doi.org/10.1002/wcms.1159.

Jain, A., Ong, S.P., Hautier, G., Chen, W., Richards, W.D., Dacek, S., Cholia, S., Gunter, D., Skinner, D., Ceder, G., Persson, K.A., 2013. Commentary: the materials project: a materials genome approach to accelerating materials innovation. APL Mater. 1. https://doi.org/10.1063/1.4812323.

Jakobtorweihen, S., Ingram, T., Smirnova, I., 2013. Combination of COSMOmic and molecular dynamics simulations for the calculation of membrane–water partition coefficients. J. Comput. Chem. 34, 1332–1340. https://doi.org/10.1002/jcc.23262.

Johnston, R.L., 2002. Atomic and Molecular Clusters. CRC Press. https://doi.org/10.1201/9780367805814.

Kamysbayev, V., Filatov, A.S., Hu, H., Rui, X., Lagunas, F., Wang, D., Klie, R.F., Talapin, D.V., 2020. Covalent surface modifications and superconductivity of two-dimensional metal carbide MXenes. Science 369, 979–983. https://doi.org/10.1126/science.aba8311.

Khazaei, M., Ranjbar, A., Arai, M., Sasaki, T., Yunoki, S., 2017. Electronic properties and applications of MXenes: a theoretical review. J. Mater. Chem. C Mater. 5, 2488–2503. https://doi.org/10.1039/C7TC00140A.

Klamt, A., 1995. Conductor-like screening model for real solvents: a new approach to the quantitative calculation of solvation phenomena. J. Phys. Chem. 99, 2224–2235. https://doi.org/10.1021/j100007a062.

Klamt, A., Jonas, V., Bürger, T., Lohrenz, J.C.W., 1998. Refinement and parametrization of COSMO-RS. J. Phys. Chem. A 102, 5074–5085. https://doi.org/10.1021/jp980017s.

Krishnamoorthy, R., Muthumalai, K., Nagaraja, T., Rajendrakumar, R.T., Das, S.R., 2022. Chemically exfoliated titanium carbide MXene for highly sensitive electrochemical sensors for detection of 4-Nitrophenols in drinking water. ACS Omega 7, 42644–42654. https://doi.org/10.1021/acsomega.2c06505.

Le, V.T., Vasseghian, Y., Doan, V.D., Nguyen, T.T.T., Thi Vo, T.-T., Do, H.H., Vu, K.B., Vu, Q.H., Dai Lam, T., Tran, V.A., 2022. Flexible and high-sensitivity sensor based on Ti3C2–MoS2 MXene composite for the detection of toxic gases. Chemosphere 291, 133025. https://doi.org/10.1016/j.chemosphere.2021.133025.

Lemena, J., Harris, R.A., Swart, H.C., Terblans, J.J., Motaung, D.E., 2025. Advances in the engineering of MXenes-based sensors: a transition towards advanced sensing technologies. Sensors Actuators B Chem. 441, 137939. https://doi.org/10.1016/j.snb.2025.137939.

Li, P., Merz, K.M., 2014. Taking into account the ion-induced dipole interaction in the nonbonded model of ions. J. Chem. Theory Comput. 10, 289–297. https://doi.org/10.1021/ct400751u.

Li, P., Merz, K.M., 2016. MCPB.Py: a python based metal center parameter builder. J. Chem. Inf. Model. 56, 599–604. https://doi.org/10.1021/acs.jcim.5b00674.

Li, P., Roberts, B.P., Chakravorty, D.K., Merz, K.M., 2013. Rational design of particle mesh ewald compatible Lennard-Jones parameters for +2 metal cations in explicit solvent. J. Chem. Theory Comput. 9, 2733–2748. https://doi.org/10.1021/ct400146w.

Li, L., Fu, X., Chen, S., Uzun, S., Levitt, A.S., Shuck, C.E., Han, W., Gogotsi, Y., 2020. Hydrophobic and stable MXene–polymer pressure sensors for wearable electronics. ACS Appl. Mater. Interfaces 12, 15362–15369. https://doi.org/10.1021/acsami.0c00255.

Lim, G.P., Soon, C.F., Ma, N.L., Morsin, M., Nayan, N., Ahmad, M.K., Tee, K.S., 2021. Cytotoxicity of MXene-based nanomaterials for biomedical applications: a mini review. Environ. Res. 201, 111592. https://doi.org/10.1016/j.envres.2021.111592.

Lin, H., Buerki-Thurnherr, T., Kaur, J., Wick, P., Pelin, M., Tubaro, A., Carniel, F.C., Tretiach, M., Flahaut, E., Iglesias, D., Vázquez, E., Cellot, G., Ballerini, L., Castagnola, V., Benfenati, F., Armirotti, A., Sallustrau, A., Taran, F., Keck, M., Bussy, C., Vranic, S., Kostarelos, K., Connolly, M., Navas, J.M., Mouchet, F., Gauthier, L., Baker, J., Suarez-Merino, B., Kanerva, T., Prato, M., Fadeel, B., Bianco, A., 2024. Environmental and health impacts of graphene and other two-dimensional materials: a graphene flagship perspective. ACS Nano 18, 6038–6094. https://doi.org/10.1021/acsnano.3c09699.

Liu, Z., Alshareef, H.N., 2021. MXenes for optoelectronic devices. Adv. Electron. Mater. 7. https://doi.org/10.1002/aelm.202100295.

Lizano-Fallas, V., Carrasco del Amor, A., Cristobal, S., 2023. Prediction of molecular initiating events for adverse outcome pathways using high-throughput identification of chemical targets. Toxics 11, 189. https://doi.org/10.3390/toxics11020189.

Lukatskaya, M.R., Kota, S., Lin, Z., Zhao, M.-Q., Shpigel, N., Levi, M.D., Halim, J., Taberna, P.-L., Barsoum, M.W., Simon, P., Gogotsi, Y., 2017. Ultra-high-rate pseudocapacitive energy storage in two-dimensional transition metal carbides. Nat. Energy 2, 17105. https://doi.org/10.1038/nenergy.2017.105.

Mansoor, N.E., Diaz, L.A., Shuck, C.E., Gogotsi, Y., Lister, T.E., Estrada, D., 2022. Removal and recovery of ammonia from simulated wastewater using Ti3C2Tx MXene in flow electrode capacitive deionization. NPJ Clean Water 5, 26. https://doi.org/10.1038/s41545-022-00164-3.

MGLTools, 2011.

Molecular Operating Environment (MOE), 2022.

Morris, G.M., Huey, R., Lindstrom, W., Sanner, M.F., Belew, R.K., Goodsell, D.S., Olson, A.J., 2009. AutoDock4 and AutoDockTools4: automated docking with selective receptor flexibility. J. Comput. Chem. 30, 2785–2791. https://doi.org/10.1002/jcc.21256.

Mortensen, J.J., Larsen, A.H., Kuisma, M., Ivanov, A.V., Taghizadeh, A., Peterson, A., Haldar, A., Dohn, A.O., Schäfer, C., Jónsson, E.Ö., Hermes, E.D., Nilsson, F.A., Kastlunger, G., Levi, G., Jónsson, H., Häkkinen, H., Fojt, J., Kangsabanik, J., Sødequist, J., Lehtomäki, J., Heske, J., Enkovaara, J., Winther, K.T., Dulak, M., Melander, M.M., Ovesen, M., Louhivuori, M., Walter, M., Gjerding, M., Lopez-Acevedo, O., Erhart, P., Warmbier, R., Würdemann, R., Kaappa, S., Latini, S., Boland, T.M., Bligaard, T., Skovhus, T., Susi, T., Maxson, T., Rossi, T., Chen, X., Schmerwitz, Y.L.A., Schiøtz, J., Olsen, T., Jacobsen, K.W., Thygesen, K.S., 2024. GPAW: an open python package for electronic structure calculations. J. Chem. Phys. 160. https://doi.org/10.1063/5.0182685.

MXene Nanosheets For Future Optoelectronic Devices, 2020. Doi: https://doi.org/10.3030/895916.

Naguib, M., Mochalin, V.N., Barsoum, M.W., Gogotsi, Y., 2014. 25th anniversary article: MXenes: a new family of two-dimensional materials. Adv. Mater. 26, 992–1005. https://doi.org/10.1002/adma.201304138.

Navarro-Cuñado, A.M., Tapia, M.J., de-la-Huerta-Sainz, S., Gutiérrez, A., Aparicio, S., 2025. In silico characterization of ciwujianoside e: structural features, solvation dynamics, and eco-toxicological assessment. Comput. Struct. Biotechnol. J. 27, 3379–3398. https://doi.org/10.1016/j.csbj.2025.07.041.

Nawaz, A., Molnárová, M., Kusumkar, V.V., Galamboš, M., Atri, S., Monfort, O., Fargašová, A., 2025. Toxicity assessment of MXene in *Scenedesmus quadricauda* physicochemical parameters. Water Air Soil Pollut. 236, 750. https://doi.org/10.1007/s11270-025-08335-x.

Pang, J., Mendes, R.G., Bachmatiuk, A., Zhao, L., Ta, H.Q., Gemming, T., Liu, H., Liu, Z., Rummeli, M.H., 2019. Applications of 2D MXenes in energy conversion and storage systems. Chem. Soc. Rev. 48, 72–133. https://doi.org/10.1039/C8CS00324F.

Perdew, J.P., Burke, K., Ernzerhof, M., 1996. Generalized gradient approximation made simple. Phys. Rev. Lett. 77, 3865–3868. https://doi.org/10.1103/PhysRevLett.77.3865.

Purbayanto, M.A.K., Jakubczak, M., Bury, D., Nair, V.G., Birowska, M., Moszczyńska, D., Jastrzębska, A., 2022. Tunable antibacterial activity of a polypropylene fabric coated with bristling Ti3C2Tx MXene flakes coupling the nanoblade effect with ROS generation. ACS Appl. Nano Mater. 5, 5373–5386. https://doi.org/10.1021/acsanm.2c00365.

Ren, C.E., Hatzell, K.B., Alhabeb, M., Ling, Z., Mahmoud, K.A., Gogotsi, Y., 2015. Charge- and size-selective ion sieving through ti 3 c 2 t x MXene membranes. J. Phys. Chem. Lett. 6, 4026–4031. https://doi.org/10.1021/acs.jpclett.5b01895.

Santos-Martins, D., Forli, S., Ramos, M.J., Olson, A.J., 2014. AutoDock4Zn: an improved AutoDock force field for small-molecule docking to zinc metalloproteins. J. Chem. Inf. Model. 54, 2371–2379. https://doi.org/10.1021/CI500209E/SUPPL_FILE/CI500209E_SI_001.PDF.

Schwö, J.A.H., Ebert, A., Bittermann, K., Huniar, U., Goss, K.-U., Klamt, A., 2020. COSMOperm: mechanistic prediction of passive membrane permeability for neutral compounds and ions and its pH dependence. J. Phys. Chem. 2020, 3354. https://doi.org/10.1021/acs.jpcb.9b11728.

Scott, D.L., White, S.P., Otwinowski, Z., Yuan, W., Gelb, M.H., Sigler, P.B., 1990. Interfacial catalysis: the mechanism of phospholipase A 2. Science 250, 1541–1546. https://doi.org/10.1126/science.2274785.

Shao, B., Liu, Z., Zeng, G., Wang, H., Liang, Q., He, Q., Cheng, M., Zhou, C., Jiang, L., Song, B., 2020. Two-dimensional transition metal carbide and nitride (MXene) derived quantum dots (QDs): synthesis, properties, applications and prospects. J. Mater. Chem. A Mater. 8, 7508–7535. https://doi.org/10.1039/D0TA01552K.

Sun, D., Wang, M., Li, Z., Fan, G., Fan, L.-Z., Zhou, A., 2014. Two-dimensional ti 3 c 2 as anode material for li-ion batteries. Electrochem. Commun. 47, 80–83. https://doi.org/10.1016/j.elecom.2014.07.026.

Thakur, A., Anasori, B., 2024. Accelerating 2D materials discovery. Science 383, 1182–1183. https://doi.org/10.1126/science.ado4113.

The MathWorks Inc, 2024a. MATLAB Version: 24.1.0.2689473 (R2024a).

The MathWorks Inc, 2024b. Statistics and Machine Learning Toolbox.

Tomić, D., Murgić, J., Fröbe, A., Skala, K., Vrljičak, A., Medved Rogina, B., Kolarek, B., Bojović, V., 2024. Exploring potential therapeutic combinations for castration-sensitive prostate cancer using supercomputers: a proof of concept study. Sci. Rep. 14, 18824. https://doi.org/10.1038/s41598-024-69880-9.

TURBOMOLE V7.8 2023, 2026.

VahidMohammadi, A., Moncada, J., Chen, H., Kayali, E., Orangi, J., Carrero, C.A., Beidaghi, M., 2018. Thick and freestanding MXene/PANI pseudocapacitive electrodes with ultrahigh specific capacitance. J. Mater. Chem. A Mater. 6, 22123–22133. https://doi.org/10.1039/C8TA05807E.

Vasyukova, I.A., Zakharova, O.V., Kuznetsov, D.V., Gusev, A.A., 2022. Synthesis, toxicity assessment, environmental and biomedical applications of MXenes: a review. Nanomaterials 12, 1797. https://doi.org/10.3390/nano12111797.

Wang, H., Zhang, J., Wu, Y., Huang, H., Li, G., Zhang, X., Wang, Z., 2016. Surface modified MXene Ti3C2 multilayers by aryl diazonium salts leading to large-scale delamination. Appl. Surf. Sci. 384, 287–293. https://doi.org/10.1016/j.apsusc.2016.05.060.

Wu, W., Ge, H., Zhang, L., Lei, X., Yang, Y., Fu, Y., Feng, H., 2020. Evaluating the cytotoxicity of Ti3C2 MXene to neural stem cells. Chem. Res. Toxicol. 33, 2953–2962. https://doi.org/10.1021/acs.chemrestox.0c00232.

Yao, Y., Li, X., Sisican, K.M., Ramos, R.M.C., Judicpa, M., Qin, S., Zhang, J., Yao, J., Razal, J.M., Usman, K.A.S., 2025. Progress towards efficient MXene sensors. Commun. Mater. 6, 210. https://doi.org/10.1038/s43246-025-00907-y.